Anomalous percolation flow transition of yield stress fluids in porous media

Nicolas Waisbord,[1,*,†] Norbert Stoop,[2,3,*] Derek M. Walkama,[1,4]
Jörn Dunkel,[2] and Jeffrey S. Guasto[1,‡]
[1]*Department of Mechanical Engineering, Tufts University, 200 College Avenue, Medford, Massachusetts 02155, USA*
[2]*Department of Mathematics, Massachusetts Institute of Technology, 77 Massachusetts Avenue, Cambridge, Massachusetts 02139-4307, USA*
[3]*Institute of Building Materials, ETH Zürich, Stefano-Franscini-Platz 3, 8093 Zürich, Switzerland*
[4]*Department of Physics and Astronomy, Tufts University, 574 Boston Avenue, Medford, Massachusetts 02155, USA*

(Received 29 May 2018; revised manuscript received 1 July 2018; published 7 June 2019)

Yield stress fluid (YSF) flows through porous materials are fundamental to biological, industrial, and geophysical processes, from blood and mucus transport to enhanced oil recovery. Despite their widely recognized importance across scales, the emergent transport properties of YSFs in porous environments remain poorly understood due to the nonlinear interplay between complex fluid rheology and pore microstructure. Here, we combine microfluidic experiments and nonlinear network theory to uncover an anomalous, hierarchical yielding process in the fluidization transition of a generic YSF flowing through a random medium. Percolation of a single fluidized filament gives way to pathways that branch and merge to form a complex flow network within the saturated porous medium. The evolution of the fluidized network with the flowing fraction of YSF results in a highly nonlinear flow conductivity and reveals a novel dispersion mechanism, resulting from the rerouting of fluid streamlines. The identified flow percolation phenomenon has broad implications for YSF transport in natural and engineered systems, and provides a tractable archetype for a diverse class of breakdown phenomena.

DOI: 10.1103/PhysRevFluids.4.063303

I. INTRODUCTION

Yield stress fluids (YSFs) encompass a broad range of materials [1–3] from whipped cream to clay suspensions to waxy crude oil. These non-Newtonian fluids exhibit an elastic response if their internal stresses are weak, but begin to flow upon exceeding a critical yield stress [1]. The fluidization of YSFs arises from microstructural transformations [1,4] in a variety of materials including emulsions, gels, suspensions, and foams. YSFs play important roles in a myriad of systems [1,5–7]. However, when flowing in confined spaces, their nonlinear rheology causes profound technological and medical problems, exemplified by the clogging of pipes in petroleum processing [3,7] and the obstruction of bronchial tubes by mucus causing infections [5]. Conversely, gastropods rely on the yield stress of a thin pedal mucus layer between their body and the substrate for locomotion [8]. Over the past two decades, much progress has been made on understanding the

*These authors contributed equally to this work.
†Corresponding author: nicolas.waisbord@gmail.com
‡Corresponding author: Jeffrey.Guasto@tufts.edu

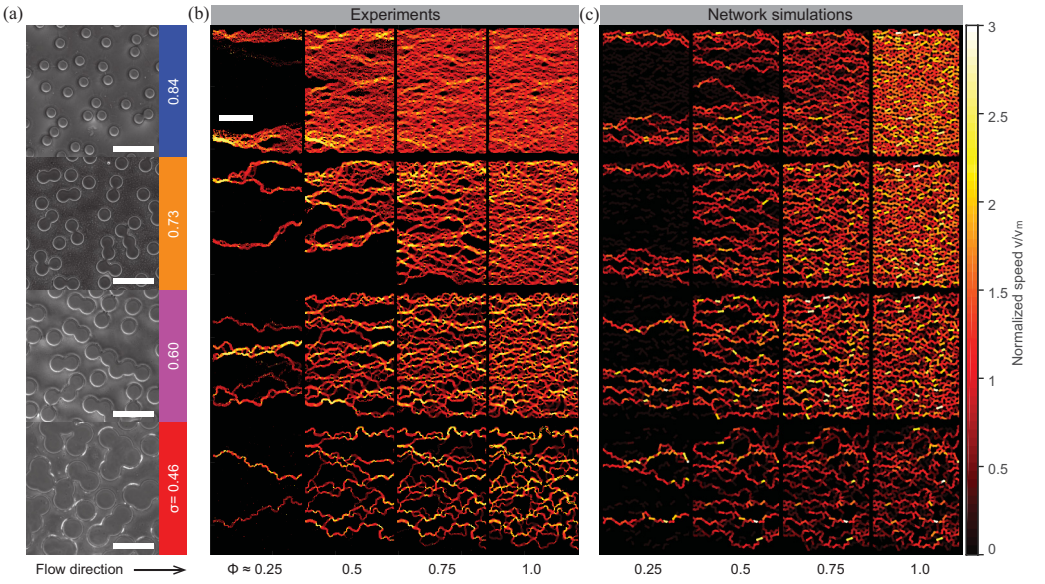

FIG. 1. Fluidization of a yield stress fluid in saturated porous media. (a) Images of microfluidic porous media channels. Porosity σ is controlled by adjusting pillar radii $r = 25$, 32.5, 40, and 47.5 μm, respectively. Pillar locations in experiments and simulations are generated by randomizing a hexagonal lattice (see also Supplemental Material [25]). Porosity color coding is carried throughout all figures. Scale bars, 250 μm. (b) Experimentally measured flow speed fields generated from particle tracking data [25]. Flow direction is from left to right in all figures. Rows correspond to the porosities in panel (a) and columns correspond to four selected yielded fractions Φ, with pressure drop ΔP increasing from left to right. Flow speed v is normalized by the median flow speed v_m for each map. Black zones are arrested microgel and pillars. Scale bar, 1 mm. (c) Flow speed maps from pore network simulations [25] for parameters corresponding to panel (b).

bulk mechanical properties of YSFs [1–3,9,10], but relatively little is known about their transport properties in geometrically complex, realistic environments beyond numerical work [11–16].

YSFs often flow through porous materials characterized by significant geometrical heterogeneity, such as soils and blood vessel networks [17]. The coexistence of fluidized and arrested yield stress material and its potential effects on fluid transport through heterogeneous porous media have not been realized experimentally [4,9,12,16], despite numerical predictions from porescale [16,18] and continuous simulations [11]. Newtonian fluid flows through porous media have been extensively studied [19,20], and are characterized by a linear transport relationship between fluid flux and applied pressure gradient, namely Darcy's Law [9]. In contrast, multiphase fluid flows through porous media exhibit a rich array of flow topologies, which are dictated by the coupling of pore geometry and material properties, for example surface tension or viscosity contrast in drainage and infiltration flows [21–23]. Here, we demonstrate through microfluidic experiments that yield stress rheology leads to the fluidization of discrete pathways that coexist with arrested, solid regions of the same material under finite applied pressure gradients (Figs. 1(a) and 1(b); see Supplemental Material for a movie [24]). The percolation and subsequent growth of the fluidized network within the porous microstructure result in strongly nonlinear transport properties. A newly developed, highly scalable, nonlocal, network-based theory [25] for YSF flows in porous media corroborates our experimental findings [Fig. 1(c)], and provides a conceptual and computational framework for future studies.

II. EXPERIMENTAL METHODS AND PORE NETWORK MODELING

A. Microfluidic model porous medium

To identify the transport characteristics of pressure-driven YSFs in disordered porous media, we designed a quasi-two-dimensional, porous microfluidic device (20 mm long, 3.6 mm wide, 35 μm high). Cylindrical pillars of radius r, placed on a randomly perturbed hexagonal lattice (see Supplemental Material [25]), control the porosity σ, which was tuned over a broad range $0.46 \leqslant \sigma \leqslant 0.84$ by adjusting the pillar radius $25 \leqslant r \leqslant 47.5$ μm [Fig. 1(a)]. Porous microfluidic devices were fabricated using standard soft lithography techniques [26]. A master mold was created using photolithography (SU-8 2025, Microchem; see Supplemental Material [25]). The mold contained four individual microchannels with identical randomized pillar arrangements but different pillar radii ($r = 25$, 32.5, 40, and 47.5 μm) corresponding to the four porosities ($\sigma = 0.46$, 0.60, 0.73, and 0.84), respectively. Polydimethylsiloxane (PDMS; Sylgard 184, Dow Corning) microchannels were cast from the mold, plasma bonded to a glass microscope slide, and reinforced on top with an additional glass slide [25] to sustain high pressures in experiments (<2 bar). Prior to experiments, the glass-reinforced microchannels were chemically treated by flowing an ethanol and water solution to ensure homogeneous microgel-surface interactions (see Supplemental Material [25]).

A canonical YSF, Carbopol microgel (ETD 2050, Lubrizol) [10,13,27], was prepared following the recipe of Geraud *et al.* [27] with dilute fluorescent microspheres (500 nm diameter) to trace the flow. Briefly, deionized water with microspheres was heated to 50 °C and mixed with Carbopol powder (0.5% w/v; 100 rpm for 30 min). The cooled solution was pH adjusted to 6.5 pH using NaOH with continuous stirring (100 rpm). The microgel suspension was then stirred (2100 rpm for 12 h) to homogenize the microgel particle sizes, and bubbles were removed via centrifugation (2000 rcf for 10 min). The yield stress behavior of the transparent microgel was measured on a cone and plate rheometer (see Supplemental Material for details [25]). The resulting flow curve for the stress, τ, versus strain rate, $\dot{\gamma}$, was fitted well by the Herschel-Bulkley model

$$\tau = \tau_c + \kappa \dot{\gamma}^n. \tag{1}$$

The resulting measured yield stress parameters for our microgel were the yield stress $\tau_c = 3.0 \pm 0.2$ Pa, the consistency index $\kappa = 1.2 \pm 0.1$ (SI units), and the flow index $n = 0.55 \pm 0.02$, which agree well with previously reported values for similar sample preparations [27]. Flow through the porous microfluidic channels was driven by a precision pressure controller (Elveflow OB-1), and after loading microchannels with YSF, the flow was arrested at 0 bar ($\Phi = 0$; 30 min). For each porous channel, the pressure drop ΔP along the channel was increased stepwise from 0 mbar to a maximum pressure in the range 600–1300 mbar, until the microgel was fully yielded ($\Phi = 1$). Each intermediate pressure was held for 20 min to ensure steady-state flow. Fluorescent tracer particle motion was captured (Nikon Ti-e; 4×, 0.13 NA objective) in 20 separate videos per pressure (30 s long, 8 frames/s; Andor Zyla). Particles were tracked using custom MATLAB codes with a predictive algorithm. Particle trajectories were smoothed using a five-point Savitzky-Golay filter, and velocity fields [Fig. 1(b)] were generated by binning tracer velocity in a regularized grid [25]. The experimental data presented here comprise the measured flow field for each applied pressure over one pressure cycle for each porosity.

B. Nonlinear pore network model

To rationalize our experiments, we perform corresponding nonlinear pore network simulations (Fig. 1(c); see also Supplemental Material [25]) [14,16]. To model the flow of the microgel, we first discretize the pore geometry into a network of nodes and edges by means of a Voronoi tesselation. In this approach, each edge corresponds to a throat between two pillars. Throats merge at pores that correspond to the nodes of the network. As suggested by experimental observations, the dominant effect of the complex microgel rheology at this scale lies in a nonlinear relationship between the volumetric flow f through an edge and the local pressure drop Δp across it. We approximate this nonlinearity by requiring edge flows $f \sim 0$ on edges with pressure drops below a

geometry-dependent local yielding pressure p^c. Conversely, we assume a power-law increase

$$f \sim (\Delta p - p^c)^{1/n}, \tag{2}$$

for edges where the pressure drop $\Delta p > p^c$ [25]. Geometry enters into the model by scaling the nonlinear pressure-flow relationship for each edge by a local hydraulic conductance k that accounts for the width and length of a throat. For each edge, the yielding pressure is calculated as

$$p^c = 4L\tau_c s/\min(H, W), \tag{3}$$

where L is the duct length, H is the height, and W is the width, respectively. For $s = 1$, p^c coincides with the yielding pressure of a YSF in a circular duct [28,29] with radius

$$R = \min(H, W)/2. \tag{4}$$

We note that our choice introduces a strong simplification of the rectangular throat cross-sectional geometry. This simplification was necessary because, to our knowledge, no closed form analytical expression for flow in a rectangular duct is available. Qualitatively, we observed the best results for the particular choice of equivalent radius, R, given in Eq. (4). As the introduced error is largest in throats with extreme aspect ratios, the qualitatively good agreement with experiments suggests that such throats typically do not participate in the flow network. In Eq. (3), we also introduced $0 < s \leqslant 1$ as an attenuation factor, which decreases as the flow in directly neighboring edges increases [25]. Consequently, p^c of an edge is reduced if neighboring edges are yielded. The attenuation factor is motivated as follows: If a physical throat yields, a minimum of two adjacent pores must also yield to allow the microgel to flow and to maintain continuity. This effect is not accounted for in a standard network model, since the nodes do not represent physical space and thus do not contribute to the yielding pressure. The attenuation factor corrects for this effect, and proved important to capture the flow topologies observed in experiments [Fig. 1(c)].

To simulate the nonlinear flow, the unknown pressure field was assigned to the nodes, and the effective flux along edges (throats) was described by the above nonlinear conductance law, based on the Herschel-Bulkley flow through a duct [25]. Inlet and outlet fluxes were prescribed for nodes at the right and left boundaries of the network, respectively. By enforcing incompressibility of the fluid at each node, a well-defined nonlinear optimization problem was obtained [25]. Starting from small inlet/outlet fluxes, MATLAB's Levenberg-Marquardt algorithm was then used to solve for the unknown pressure field and edge fluxes, closely mimicking the experimental protocol.

III. RESULTS AND DISCUSSION

A. Yield stress fluid percolation transition in porous media

As the pressure drop increases from 0 mbar, the microgel locally yields at a small but finite pressure drop $\Delta P_c > 0$, indicative of its yield stress rheology (Fig. 1(b); see Supplemental Material for a movie [24]). The yielded volume fraction Φ quantifies the relative amount of fluidized material. Upon yielding, continuity requires the fluidized phase of the microgel to percolate across the medium. Consequently, for the flow to set in a specific location of the channel, not only does the pressure gradient needs to surpass a local threshold associated with the local geometry, but it needs to be part of a global subset of the network where this condition is fulfilled. Strikingly, the flow is initially supported by only a few discrete fluidized pathways, whereas the bulk of the material remains in the solid phase [$\Phi \approx 0.25$; Fig. 1(b)]. Upon further increasing the pressure, the network of fluidized paths grows [$\Phi \approx 0.5, 0.75$; Fig. 1(b)], eventually overtaking the entire pore space of the medium ($\Phi \approx 1.0$; Fig. 1). Predictions from our pore network simulations agree well with these observations [Fig. 1(c)], and the yielding characteristics persist across the four different porosities examined. However, the topology of the fluidized pathways changes notably with porosity. At high porosity, channelized flow paths can span several pores immediately following the percolation transition [$\sigma = 0.84$; Figs. 1(b) and 1(c)], meanwhile at low porosity, well-separated, individual

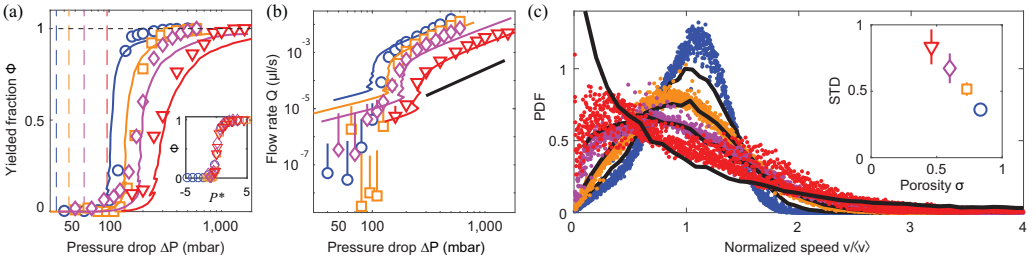

FIG. 2. Coexistence of yielded and arrested regions reveals the nature of nonlinear conductivity in porous media. Color coding for the different porosities is defined in Fig. 1. (a) Yielded fraction Φ of microgel, measured from flow speed maps [Fig. 1(b) and 1(c)], transitions smoothly from 0 to 1 with increasing pressure drop ΔP. Symbols are experimental data measured from individual flow field realizations, solid lines are predictions from pore network simulations, and vertical dashed lines are scaling predictions for percolation onset pressure. Color coding for the different porosities is defined in Fig. 1. Inset: Collapse of the fluidization transition for all porosities with nondimensional pressure P^*. (b) Total flow rate Q, computed from individual measured velocity fields, increases nonlinearly with pressure drop for the four different porosities. The black line indicates expected asymptotic slope $1/n \approx 1.8$ from the shear-thinning rheology of the microgel. Error bars indicate standard deviation of flow rates measured at different cross sections along the microchannel for a single measured flow field per data point, where some error bars are occluded by the data points. (c) Flow speed distributions for the flow maps in Fig. 1(b). For each porosity, the normalized speed distributions for all yielded fractions $\Phi \geqslant 0.1$ collapse (mean flow speed $\langle v \rangle$). Black lines are normalized speed distributions for a Newtonian fluid (50% wt. aqueous glycerol) measured in the same microchannels. Inset: Standard deviations of YSF flow speed probability density functions (PDFs) with error bars indicating the variation for different yielded fractions within a porosity.

flow paths are observed [$\sigma = 0.46$; Fig. 1(b) and 1(c)], indicating a complex interplay between the porous geometry and nonlinear fluid rheology.

B. Coexistence of fluidized and arrested phases

Macroscopically, the transition from arrested to fully yielded flow is characterized by a smooth increase of the yielded volume fraction Φ with increasing pressure difference ΔP [Fig. 2(a)]. While the yielding onset and slope vary with porosity σ, the sigmoidal shape of the transition in Φ is universal [Fig. 2(a), inset]. We identify three distinct regimes in qualitative agreement with predictions from earlier Lattice-Boltzmann simulations [12]: (*i*) For small pressure drops, the entire microgel remains unyielded with $\Phi = 0$. (*ii*) Once the yielding transition begins, Φ increases continuously ($0 < \Phi < 1$) with ΔP over a finite range of pressure drops. (*iii*) Beyond this range of pressure drops, the entire microgel yields, and the yielded fraction saturates at $\Phi = 1$ [Fig. 2(a)]. We emphasize that, in contrast to the discontinuous jump of the yielded fluid fraction for a single duct [27], the fluidization transition in porous media is smooth over a wide range of pressure drops, and exhibits a universal behavior across the inspected range of porosities [Fig. 2(a), inset]. The applied pressure ΔP was nondimensionalized as P^* by rescaling $P^* = (\Delta P - \Delta P|_{\Phi=0.5}) \times d\Phi/d\Delta P|_{\Phi=0.5}$. The transition pressure $\Delta P|_{\Phi=0.5}$ at which 50% of the material is yielded and the slope of the fluidization transition $d\Phi/d\Delta P|_{\Phi=0.5}$ at the transition pressure were evaluated by fitting splines to the experimental data.

The onset pressure ΔP_c of the percolation flow transition increases with decreasing porosity [Fig. 2(a)]. The onset pressure difference can be estimated by assuming that, upon percolation, the YSF flows through a single, effective duct with length L set to the length of the medium ($L = 20$ mm) and porosity-dependent radius R, approximated from a hexagonal pillar lattice. For the lattice spacing $a = 120$ μm and pillar radius $r(\sigma)$, the duct radius is $R \approx [a - 2r(\sigma)]/2$. The estimated onset pressure [28] is thus $\Delta P_c = 2\tau_c L/R$, which predicts $\Delta P_c = \{34\,\text{mbar}, 44\,\text{mbar},$

60 mbar, 96 mbar} for porosities $\sigma = \{0.84, 0.73, 0.60, 0.46\}$. These simple estimates correspond to the observed onset of the yielding process [Fig. 2(a)].

C. Partial yielding drives an additional nonlinear bulk conductivity regime

Selective yielding, caused by geometrical inhomogeneities in the porous medium, results in a highly nonlinear hydraulic conductivity. During the yielding transition, the measured volumetric flow rate Q increases rapidly with ΔP before approaching an asymptotic regime at large pressures [Fig. 2(b)]. The nonlinear increase in Q is rationalized as follows: Just beyond the critical pressure $\Delta P > \Delta P_c$, the YSF undergoes the yielding transition ($0 < \Phi < 1$), where two effects conspire to dramatically increase the flow rate [12]. An increase in ΔP increases the flux along existing fluidized pathways and simultaneously yields new pathways [Fig. 2(b)]. For sufficiently large ΔP beyond the yielding transition ($\Phi = 1$), no additional pathways are available. The conductivity decreases and approaches Darcy's law, $Q \sim (\Delta P/L)^{1/n}$, which reflects the shear thinning behavior of the microgel, $\tau \sim \dot{\gamma}^n$ [black line, $1/n \approx 1.8$; Fig. 2(b)] [4,27,30]. Thus, in a porous medium, the macroscopic flow rate Q in the fully yielded regime behaves as a YSF flow in a simple duct [13,27]. However, in the partially yielded transitional regime, Q exhibits a strongly nonlinear dependence on ΔP, due to the geometrical disorder of the porous medium [12,18,31].

D. Pore geometry dominates flow statistics

To further elucidate the interplay between rheology and geometry, we analyze the flow speed distributions in the porous medium [Fig. 2(c)]. In addition to its yield stress, the microgel is shear thinning [27]. Yet, for a given porosity, the probability distributions of normalized flow speed $v/\langle v\rangle$ collapse onto a single curve for all yielded fractions [Fig. 2(c)]. Surprisingly, we observe similar speed distributions for a Newtonian fluid [32] [Fig. 2(c), black curves], indicating that variations in the pore geometry, not rheology, dictate flow speed statistics [20,30]. Moreover, the invariance of the speed distributions throughout the yielding transition implies that the initially filamentous flow at the onset of percolation uniformly samples the distribution of throat conductivity in the porous network. As path yielding is dictated by overall resistivity, the emergent path structure may be dominated by a few, statistically rare, high-resistance throats. Flow speed distributions are insensitive to such rare events, which would not impact their shape throughout the yielding process.

E. Pressure cycling reveals hysteresis of the yielded fraction

Despite the known shortcomings of bulk rheological models to capture finite size and surface effects in YSF flows [27], the scaling arguments and pore network simulations presented above perform strikingly well in quantifying fluid transport during the fluidization transition in porous media. Signatures of these effects, including yielding transition hysteresis and partial slip, are indeed present our system. While they add to the richness of the yielding process, their presence also reinforces the robustness of our analysis, based on a nonslip Herschel-Bulkley model [28], to quantitatively characterize the system's transport properties.

Upon cycling of the applied pressure drop, the fluidization transition, characterized by the yielded fraction, exhibits hysteresis, which is not predicted by simple rheological models (Fig. 3). In particular, yielding the microgel requires a pressure drop that is a factor of $\approx$2 larger compared to the pressure drop at which resolidification occurs for $\Phi = 0.5$. Unlike thixotropic laponite suspensions, bulk rheological hysteresis is generally not observed in Carbopol, due to the relatively fast reconfiguration time of the microgel [33]. Rather, we hypothesize that the yielded fraction hysteresis observed here stems from polymer granularity and surface slip (Fig. 4), since the throat size is 5 to 8 times larger than the reported microgel particle size [34]. High resolution velocity field measurements at the pore scale [Fig. 4(a)] revealed that yielded microgel exhibits little to no slip along unyielded microgel domains, but has significant partial slip in the vicinity of PDMS pillars [Fig. 4(b)], where the latter is well established for microgels [1,35]. Focused on the coarser,

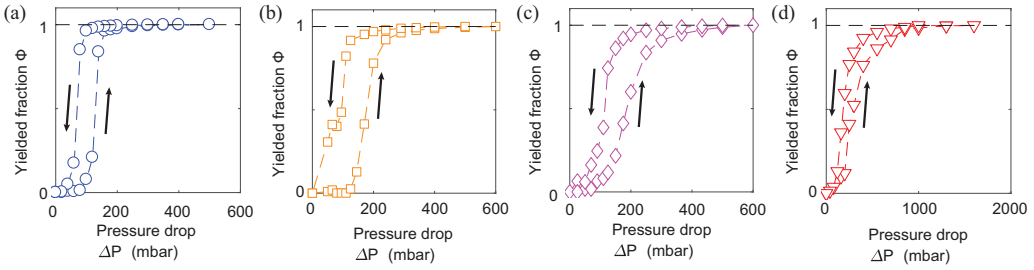

FIG. 3. Yielded fraction of flowing microgel exhibits hysteresis upon pressure cycling. Experiments are performed by ramping pressure up from 0 mbar to a maximum applied pressure, then back to 0 mbar. Upon cycling the applied pressure, a hysteresis of the flowing fraction Φ is observed for all porosities: (a) $\sigma = 0.84$, (b) $\sigma = 0.73$, (c) $\sigma = 0.60$, and (d) $\sigma = 0.46$.

hydraulic network scale, our pore-network model, based on the macroscale bulk rheology of the microgel and non-slip models of the flow in simplified ducts, overlooks these nuanced microscale effects, and yet accurately predicts the topological characteristics of the ramified flow field observed in experiments.

F. Partial yielding reroutes flow paths

Due to the strong dependence of flow topology on porous geometry, we expect that the dispersive properties of the YSF flow evolve as the effective pore structure changes with the yielded fraction. Dispersion in viscosity-dominated, low Reynolds number, Newtonian flows through porous media is well documented [20,36,37]. In such flows, the flow topology is invariant with changes in pressure, and the flow rate increases linearly with ΔP, thus preserving the hydrodynamic dispersion properties of the system [19,38]. In contrast, the nonlinear rheology of YSFs enables the breakdown of throat resistance and subsequent activation of new pores with increasing pressure drop. The result is a complex, effective microstructure [Fig. 5(a)] that evolves with applied pressure. We demonstrate that this phenomenon modifies the Lagrangian transport properties both at the pore scale [Figs. 5(b)–5(d)] and the network scale [Figs. 5(e) and 5(f)].

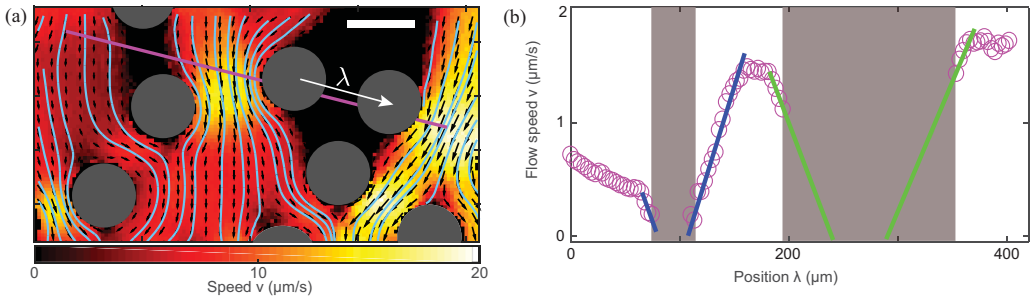

FIG. 4. Flowing microgel exhibits no slip along unyielded microgel, but shows significant partial slip on solid PDMS surfaces. (a) Flow field through a porous network ($\sigma = 0.84$, $\Phi \approx 0.5$) reconstructed from high resolution particle tracking. Gray circles represent the pillars, and black zones indicate unyielded microgel. The color map shows the measured flow speed, and light blue lines are streamlines. The magenta line corresponds to the velocity profile transect in (b) with the white arrow indicating the positive λ direction. Scale bar, 65 μm. (b) Velocity profile corresponding to the magenta transect in (a), where blue and green lines are linear fits to five points of the velocity profile near unyielded microgel and PDMS pillars, respectively. Intersections of the fits with the lateral axis show minimal slip length for the microgel, but significant slip length ($\ell_{\text{slip}} \sim 50$ μm) along the PDMS surfaces.

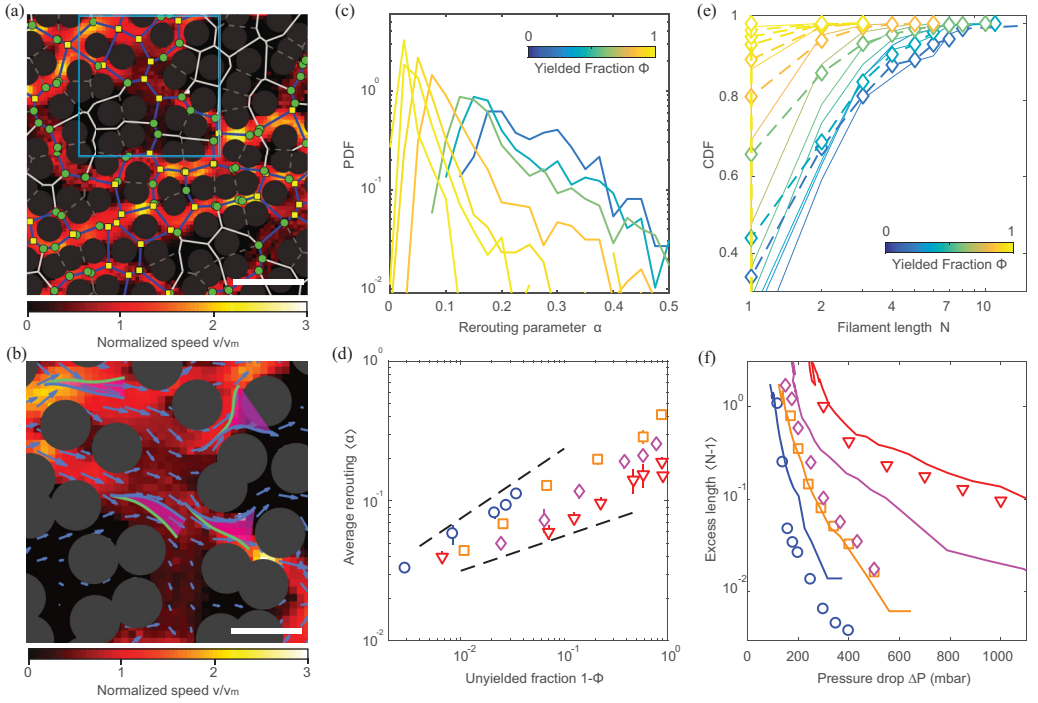

FIG. 5. Flow network topology and transport evolve with yielding. (a) Representative example of an experimentally measured pore-network exhibiting filamentous flow path topology ($\sigma = 0.62$, $\Phi = 0.60$, $\Delta P =$ 200 mbar). Pores are vertices of the Voronoi tessellation and connected by active (blue) or inactive (white) throats (edges). Throat activity is determined from the underlying measured flow speed map. Grey dashed edges are permanently inactive due to pillar merging (grey filled circles). Filaments are defined as contiguous chains of active edges connecting degree-2 vertices (green circles) and capped by degree-3 vertices (yellow squares). Cyan box indicates region shown in (b). Scale bar, 250 μm. (b) Comparison of fluid streamlines at $\Phi = 0.60$ ($\Delta P = 200$ mbar; green) and $\Phi = 1.0$ ($\Delta P = 600$ mbar; blue) illustrating the rerouting of flow during the yielding transition. Streamlines are one mean lattice spacing ($a = 120$ μm). Rerouting is quantified by $\alpha = A/a^2$, where A is the magenta shaded area bounded by streamlines at $\Phi = 0.60$ and $\Phi = 1.0$. Blue arrows show the velocity field for $\Phi = 1.0$. Scale bar, 125 μm. (c) Probability distribution of the measured rerouting parameter α for various yielded fractions Φ at fixed porosity $\sigma = 0.62$. (d) Mean rerouting parameter $\langle\alpha\rangle$ from (c) as a function of the unyielded fraction $1 - \Phi$. Error bars are standard deviations of five random subsamplings of the data, where some error bars are occluded by the data points. Dashed lines have slopes 1/2 and 1/4, respectively. (e) Cumulative distribution functions (CDFs) of fluidized filament length from the experimentally measured pore network (dashed lines and symbols) and from simulations (solid lines) for $\sigma = 0.73$. (f) Evolution of the average excess filament length $\langle N - 1\rangle$ with pressure drop in experiments (symbols) and pore-network simulations (lines).

At the pore scale, changes in transport during the yielding transition are quantified by comparing streamlines in the fluidized phase of the partially yielded microgel to streamlines in the fully yielded flow [for example $\Phi = 0.6$ and $\Phi = 1.0$; Fig. 5(b)]. Streamline rerouting is quantified by the parameter $\alpha = A/a^2$, where A is the measured area subtended between two streamlines emanating from the same location for $\Phi < 1$ and $\Phi = 1$, respectively [Fig. 5(b)]. In contrast to Newtonian fluids, an increase in pressure drop leads to fluidization of previously arrested pores and enables fluid particles to explore new regions of the porous medium. Convergence towards the fully yielded flow topology ($\Phi \to 1$) is reflected by a narrowing of the distribution of α [Fig. 5(c)] and a decrease in the average value $\langle\alpha\rangle$ [Fig. 5(d)]. Once fully yielded, the streamlines remain invariant upon

further increases of ΔP, in line with Newtonian porous media flows [19]. Thus, changes in the Lagrangian transport are dominated by the yielding process rather than the subsequent viscous rate dependence.

G. Yielded hydraulic network transitions from filamentous to branched topology

At the network scale, we study how pores (vertices) become fluidized and connected by an increasing number of active throats [edges; Fig. 5(a), blue] during the yielding transition. The measured flow field is projected onto the discretized, underlying pore network using Voronoi tessellation [Fig. 5(a); see also Supplemental Material [25]]. This mapping enables direct comparison of the flowing pore network structure between experiments and simulations. Network theory has yielded fundamental insights into complex percolation [39] and flow [20,40] phenomena. These concepts are assimilated here through the analysis of a novel physical and simulated model system [25]. In both experiments and simulations, at low to intermediate yielded fraction, the flow network is dominated by long, nonbranching filaments, defined as sequences of edges connecting degree-2 vertices [Fig. 5(a), green circles]. In this regime [$\Phi \lesssim 0.5$, $\sigma = 0.60$; Fig. 5(e)], filaments of length $N \geqslant 2$ are the primary transport conduits of the fluidized network [Fig. 1(b)], along which the fluid velocity remains strongly correlated [38] [Fig. 5(a)]. However, as $\Phi \to 1$, additional edges become activated, leading to dendritic flow topologies [Fig. 1(b)]. This branching process is characterized by an increase in the average vertex degree and a subexponential decrease of the average excess filament length $\langle N - 1 \rangle$ with increasing pressure [Fig. 5(f)].

IV. CONCLUSION

In spite of the homogeneously random microstructure, fluid transport at intermediate yielded fractions is dominated by the heterogeneous, *effective* pore structure of the emergent, filamentous flowing network. In porous media and numerous other systems, the introduction of such geometric heterogeneity is known to increase dispersive properties [36,37,41], due to enhanced spatial and temporal correlation. Thus, the strong persistence and lack of bifurcating streamlines within the filamentous flows identified here is expected to drastically augment dispersion [36,38,42], especially for small Φ. Control of the dispersive properties, via the topology of the flowing fraction, opens new avenues for anomalous transport in YSF flows, in particular for non-Brownian particles such as suspensions and microbes [43].

Our experimental and theoretical results demonstrate that the coupling between yield stress rheology and geometry gives rise to striking flow topology and nonlinear transport, as the yielded, flowing fraction percolates through the porous media. The rerouting of fluid streamlines, in response to pressure changes, reveals a novel dispersal mechanism not observed in viscous Newtonian flows. While this two-dimensional model system has provided fundamental insights into YSF flows, the higher pore connectivity in three-dimensional systems may reveal unforeseen topological transitions in the fluid network, as well as new dispersion and mixing mechanisms [38]. Furthermore, YSFs often exhibit creep and other complex rheologies [1], potentially blurring the idealized distinction of the fluidized network and augmenting transport over long time scales, which is relevant to geophysical processes [6]. From a practical perspective, our findings have immediate implications for industrial and natural applications [1,5,9,44] including remediation, extraction, filtration, and biofilms [45] in porous media. The porous YSF flows studied here illustrate a novel class of physically tractable systems that add to the diversity of percolation [15,26,28,39] and breakdown phenomena [31,46,47] in complex dynamical networks.

ACKNOWLEDGMENTS

We thank R. Juanes, T. Divoux, and B. Geraud for helpful discussions, and Y. Jin for assistance with preliminary experiments. This work was funded by NSF awards CBET-1511340 (J.S.G.),

CAREER-1554095 (J.S.G.), and CBET-1510768 (J.D.), a Complex Systems Scholar Award from the James S. McDonnell Foundation (J.D.), and Swiss National Science foundation (SNF) Grant No. IZKS2-162190.

[1] D. Bonn, M. M. Denn, L. Berthier, T. Divoux, and S. Manneville, Yield stress materials in soft condensed matter, Rev. Mod. Phys. **89**, 035005 (2017).
[2] P. Coussot, Q. D. Nguyen, H. T. Huynh, and D. Bonn, Avalanche Behavior in Yield Stress Fluids, Phys. Rev. Lett. **88**, 175501 (2002).
[3] J. Dimitriou and G. H. McKinley, A comprehensive constitutive law for waxy crude oil: A thixotropic yield stress fluid, Soft Matter **10**, 6591 (2014).
[4] G. Ovarlez, Q. Barral, and P. Coussot, Three-dimensional jamming and flows of soft glassy materials, Nat. Mater. **9**, 115 (2010).
[5] J. V. Fahy and B. F. Dickey, Airway mucus function and dysfunction, N. Engl. J. Med. **363**, 2233 (2010).
[6] J. E. Reber, L. L. Lavier, and N. W. Hayman, Experimental demonstration of a semi-brittle origin for crustal strain transients, Nat. Geosci. **8**, 712 (2015).
[7] A. Aiyejina, D. P. Chakrabarti, A. Pilgrim, and M. K. S. Sastry, Wax formation in oil pipelines: A critical review, Int. J. Multiphase Flow **37**, 671 (2011).
[8] R. H. Ewoldt, C. Clasen, A. E. Hosoi, and G. H. McKinley, Rheological fingerprinting of gastropod pedal mucus and synthetic complex fluids for biomimicking adhesive locomotion, Soft Matter **3**, 634 (2007).
[9] P. Coussot, Yield stress fluid flows: A review of experimental data, J. Non-Newtonian Fluid Mech. **211**, 31 (2014).
[10] D. D. O. dos Santos, S. L. Frey, M. F. Naccache, and P. R. de Souza Mendes, Flow of elasto-viscoplastic liquids through a planar expansion-contraction, Rheol. Acta **53**, 31 (2014).
[11] T. Chevalier and L. Talon, Generalization of Darcy's law for Bingham fluids in porous media: From flow-field statistics to the flow-rate regimes, Phys. Rev. E **91**, 023011 (2015).
[12] L. Talon and D. Bauer, On the determination of a generalized Darcy equation for yield-stress fluid in porous media using a Lattice-Boltzmann TRT scheme, Eur. Phys. J. E **36**, 139 (2013).
[13] T. Chevalier, C. Chevalier, X. Clain, J. C. Dupla, J. Canou, S. Rodts, and P. Coussot, Darcy's law for yield stress fluid flowing through a porous medium, J. Non-Newtonian Fluid Mech. **195**, 57 (2013).
[14] C. B. Shah and Y. C. Yortsos, Aspects of flow of power-law fluids in porous media, AIChE J. **41**, 1099 (1995).
[15] H. Kharabaf and Y. C. Yortsos, Invasion percolation with memory, Phys. Rev. E **55**, 7177 (1997).
[16] M. Chen, W. Rossen, and Y. C. Yortsos, The flow and displacement in porous media of fluids with yield stress, Chem. Eng. Sci. **60**, 4183 (2005).
[17] J. Goldstone, H. Schmid-Schönbein, and R. Wells, The rheology of red blood cell aggregates, Microvasc. Res. **2**, 273 (1970).
[18] S. Roux and H. J. Herrmann, Disorder-induced nonlinear conductivity, Europhys. Lett. **11**, 1227 (1987).
[19] P. G. Saffman, A theory of dispersion in a porous medium, J. Fluid Mech. **6**, 321 (1959).
[20] K. Alim, S. Parsa, D. A. Weitz, and M. P. Brenner, Local Pore Size Correlations Determine Flow Distributions in Porous Media, Phys. Rev. Lett. **119**, 144501 (2017).
[21] C. Cottin, H. Bodiguel, and A. Colin, Drainage in two-dimensional porous media: From capillary fingering to viscous flow, Phys. Rev. E **82**, 046315 (2010).
[22] R. T. Armstrong, J. E. McClure, M. A. Berrill, M. Rücker, S. Schlüter, and S. Berg, Beyond Darcy's law: The role of phase topology and ganglion dynamics for two-fluid flow, Phys. Rev. E **94**, 043113 (2016).
[23] B. Zhao, C. W. MacMinn, and R. Juanes, Wettability control on multiphase flow in patterned microfluidics, Proc. Natl. Acad. Sci. (USA) **113**, 10251 (2016).
[24] See Supplemental Material at http://link.aps.org/supplemental/10.1103/PhysRevFluids.4.063303 for animated movie of the reconstructed flow field during the percolation transition as the pressure dropped is increased.

[25] See Supplemental Material at http://link.aps.org/supplemental/10.1103/PhysRevFluids.4.063303 for details about the experimental and numerical methods.
[26] S. Davis, P. Trapman, H. Leirs, M. Begon, and J. A. P. Heesterbeek, The abundance threshold for plague as a critical percolation phenomenon, Nature (London) **454**, 634 (2008).
[27] B. Geraud, L. Bocquet, and C. Barentin, Confined flows of a polymer microgel, Eur. Phys. J. E **36**, 30 (2013).
[28] M. T. Balhoff and K. E. Thompson, Modeling the steady flow of yield-stress fluids in packed beds, AIChE J. **50**, 3034 (2004).
[29] R. P. King, *Introduction to Practical Fluid Flow* (Elsevier, New York, 2002).
[30] F. Zami-Pierre, R. De Loubens, M. Quintard, and Y. Davit, Transition in the Flow of Power-Law Fluids through Isotropic Porous Media, Phys. Rev. Lett. **117**, 074502 (2016).
[31] H. E. Stanley and P. Meakin, Multifractal phenomena in physics and chemistry, Nature (London) **335**, 405 (1988).
[32] T. Chevalier, S. Rodts, C. Chevalier, and P. Coussot, Quantitative exploitation of PFG NMR and MRI velocimetry data for the rheological study of yield stress fluid flows at macro- and micro-scales in complex geometries, Exp. Fluids **56**, 1868 (2015).
[33] T. Divoux, V. Grenard, and S. Manneville, Rheological Hysteresis in Soft Glassy Materials, Phys. Rev. Lett. **110**, 018304 (2013).
[34] L. Baudonnet, J. L. Grossiord, and F. Rodriguez, Effect of dispersion stirring speed on the particle size distribution and rheological properties of three carbomers, J. Dispersion Sci. Technol. **25**, 183 (2004).
[35] S. P. Meeker, R. T. Bonnecaze, and M. Cloitre, Slip and Flow in Soft Particle Pastes, Phys. Rev. Lett. **92**, 198302 (2004).
[36] P. K. Kang, P. de Anna, J. P. Nunes, B. Bijeljic, M. J. Blunt, and R. Juanes, Pore-scale intermittent velocity structure underpinning anomalous transport through 3-D porous media, Geophys. Res. Lett. **41**, 6184 (2014).
[37] A. Tyukhova, M. Dentz, W. Kinzelbach, and M. Willmann, Mechanisms of anomalous dispersion in flow through heterogeneous porous media, Phys. Rev. Fluids **1**, 074002 (2016).
[38] D. R. Lester, G. Metcalfe, and M. G. Trefry, Is Chaotic Advection Inherent to Porous Media Flow? Phys. Rev. Lett. **111**, 174101 (2013).
[39] R. M. D'Souza and J. Nagler, Anomalous critical and supercritical phenomena in explosive percolation, Nat. Phys. **11**, 531 (2015).
[40] D. M. Abrams, A. E. Lobkovsky, A. P. Petroff, K. M. Straub, B. McElroy, D. C. Mohrig, A. Kudrolli, and D. H. Rothman, Growth laws for channel networks incised by groundwater flow, Nat. Geosci. **2**, 193 (2009).
[41] S. Marbach, K. Alim, N. Andrew, A. Pringle, and M. P. Brenner, Pruning to Increase Taylor Dispersion in *Physarum polycephalum* Networks, Phys. Rev. Lett. **117**, 178103 (2016).
[42] J. Bear, *Dynamics of Fluids in Porous Media* (Dover, Mineola, NY, 1975).
[43] R. Rusconi, J. S. Guasto, and R. Stocker, Bacterial transport suppressed by fluid shear, Nat. Phys. **10**, 212 (2014).
[44] M. A. Nilsson, R. Kulkarni, L. Gerberich, R. Hammond, R. Singh, E. Baumhoff, and J. P. Rothstein, Effect of fluid rheology on enhanced oil recovery in a microfluidic sandstone device, J. Nonnewton. Fluid Mech. **202**, 112 (2013).
[45] L. Hall-Stoodley, J. W. Costerton, P. Stoodley, Bacterial biofilms: From the natural environment to infectious diseases, Nat. Rev. Microbiol. **2**, 95 (2004).
[46] J. Nittman, G. Daccord, and H. E. Stanley, Fractal growth of viscous fingers: Quantitative characterization of a fluid instability phenomenon, Nature (London) **314**, 141 (1985).
[47] L. Pietronero and H. J. Wiesmann, Stochastic model for dielectric breakdown, J. Stat. Phys. **36**, 909 (1984).